Received: 17 December 2021 | Revised: 15 February 2022 | Accepted: 16 February 2022

DOI: 10.1111/ffe.13686

SPECIAL ISSUE ARTICLE

FFEMS Fatigue & Fracture of Engineering Materials & Structures WILEY

Characterization of non-planar crack tip displacement fields using a differential geometry approach in combination with 3D digital image correlation

Alonso Camacho-Reyes[1] | **Jose M. Vasco-Olmo**[1] | **M. Neil James**[2,3] | **Francisco A. Diaz**[1]

[1]Departamento de Ingeniería Mecánica y Minera, Universidad de Jaén, Jaén, Spain

[2]School of Engineering, University of Plymouth, Plymouth, UK

[3]Department of Mechanical Engineering, Nelson Mandela Metropolitan University, Port Elizabeth, South Africa

Correspondence
Alonso Camacho-Reyes, Departamento de Ingeniería Mecánica y Minera, Universidad de Jaén, Jaén, Spain.
Email: acreyes@ujaen.es

Funding information
Junta de Andalucía, Grant/Award Number: 1380786

Abstract

This paper describes a novel differential geometry method that is used in combination with 3D digital image correlation (3D-DIC) for crack tip field characterization on non-planar (curved) surfaces. The proposed approach allows any of the two-dimensional crack tip field models currently available in the literature to be extended to the analysis of a 3D developable surface with zero Gaussian curvature. The method was validated by analyzing the crack tip displacement fields on hollow thin-walled cylindrical specimens, manufactured from either 304L or 2024-T3 alloy that contained a central circumferential crack. The proposed approach was checked via a comparison between experimentally measured displacement fields (3D-DIC) and those reconstructed from a modified 2D crack tip model (utilizing either 2, 3, or 4 terms of the William's expansion series) and implementing a 3D geometrical correction. Further validation was provided by comparing model-derived stress intensity factors with values provided by empirical correlations.

KEYWORDS

3D-DIC, crack tip field, curved circumferential crack, differential geometry, non-planar surface

1 | INTRODUCTION

Optimized design of mechanical components requires guarantees of their in-service structural integrity performance over the complete lifetime. This implies associated development of accurate methods of analysis that reduces their behavioral uncertainty. Cracks, or crack-like defects, are endemic in mechanical elements, and their existence can lead to catastrophic failures, particularly from fatigue processes.[1] Evaluation of the severity of a defect or crack is based on characterization of the crack tip stress/strain distributions, and a number of different mathematical models, based on various singular crack tip parameters, are available in the literature.[2–9] Many of the mathematical models, such as Westergaard's classical equations,[2,3] Williams' series expansion,[4] or Muskhelishvili's complex potentials,[6,7] are based on linear elastic fracture mechanics (LEFM). However, there

some other models, for example, those due to Hutchinson[5] or Pommier and Hamman[8] that assume an elastoplastic material behavior. More recently, a mathematical approach based on Muskhelishvili's complex potentials has been developed by Christopher, James, and Patterson, that is referred to in the literature as the CJP model.[9] It considers the potential influences on the surrounding elastic field of the plastic enclave around the tip and flanks of a fatigue crack. This opens up the possibility of directly assessing the influence of shielding mechanisms during fatigue crack growth.[10] The singularity characterization parameters that are given by most models can be successfully determined by combining the mathematical description of the crack tip field with experimental measurements obtained using full-field optical techniques. Descriptions of such techniques are given in Brewster[11] (digital photo-elasticity), Schreier et al[12] (digital image correlation [DIC]), and Thomson[13] (thermoelastic stress analysis [TSA]), and they allow direct analysis of the crack tip fields, and hence evaluation of the driving force for fatigue crack advance,[14,15] or the assessment of crack shielding phenomena.[16–18] All of these models have their origin in the differential equations of the theory of elasticity and simplify the situation to a planar geometry under 2D plane stress or plane strain conditions. The crack tip field is then generally defined by a set of polar coordinates (origin at the crack tip) in the crack plane together with the respective characterization parameters. This limitation of the models to the analysis of flat surfaces, and consequently planar components, is a major restriction in their more general applicability.

Consequently, there is a very limited number of research works in the literature in which such 2D models have been employed for the analysis of non-planar cracked surfaces. In such cases, important assumptions are made to provide an approximation to the real crack tip field at the surface. Mokhtarishirazabad et al[19] employed 2D-DIC with a high magnification lens, to calculate the stress intensity factor (SIF) from the Williams equations in an analysis of a cracked cylindrical surface. This approximate approach was valid when the magnification was sufficiently high over a small analysis zone, that the surface curvature could be neglected. However, the presence of the near crack tip plastic enclave constituted a major limitation on this approach as the authors used a linear elastic crack tip model. In essence, only data from the plastic enclave could be captured at this resolution while any plasticity effects are explicitly excluded when using a linear elastic crack tip model. To rectify this anomaly, the analysis has to be focused on the elastic zone which requires a decrease in the spatial resolution, where the effect of specimen curvature can no longer be neglected. In more recent work, Vormwald et al[20] employed 3D-DIC for the analysis of crack tip displacements; however, they also assumed a hypothetical negligible curvature with very high magnification, in order to infer SIFs using a 2D crack tip model in a thin-walled cylindrical tube under mixed mode loading.

The current work advances the characterization of curved surfaces by outlining a novel experimental approach for crack field quantification based on non-planar bodies in combination with 3D digital image correlation (3D-DIC). The method is based on a modified two-dimensional planar model using a differential geometry formulation to account for the 3D shape of the surface. In this way, a generalized plane stress crack field description for non-flat surfaces can be obtained at the surface of the specimen. The proposed methodology was applied to the analysis of crack tip displacement fields on the surface of hollow cylindrical specimens with a wall thickness of 2.11 mm made from either 304-L stainless steel or 2024-T3 aluminum alloy. Specimens contained starter notches in the form of central circumferential holes on opposite sides of the specimen with crack-like sawn extensions at their equatorial plane (illustrated in Figure 3). The accuracy of the proposed approach was assessed by comparing the displacement field measured using 3D-DIC, with that reconstructed by using a modified 2D Williams' model (with either 2, 3, or 4 terms) with a 3D geometrical correction. The observed average fitting error was lower that 0.15%, highlighting the capability of the approach in characterizing the crack tip field at the surface of a non-planar geometry. SIFs were determined at maximum load for various crack lengths and compared with empirical correlations available in the literature for this geometry.[21–23] Experimental and modeling results showed a high level of agreement, with an average error lower than 5%. Finally, to illustrate the robustness of the proposed methods, the plane stress assumption made at the specimen surface was experimentally demonstrated to be valid from an analysis of displacement components at the specimen surface, again using 3D-DIC.

This technique has significant potential in application areas that include identifying empirical fatigue crack growth relationships and determining the effective driving force for crack growth using advanced crack tip field models that incorporate influences of plasticity-induced shielding. Fatigue and fracture models developed for planar surfaces can now be extended to curved surfaces. There is also potential for application to problems of crack propagation direction, as the analysis presented has been developed for Mode I, but could be extended to include Modes II and III, allowing the likelihood of crack deflections to be predicted from the SIF changes.

2 | FUNDAMENTAL THEORY

2.1 | Williams crack tip field model

The Williams expansion series[4] is widely recognized inside the fatigue and fracture community as a reliable model that approximates the crack tip field on a flat cracked surface. According to this model, the displacement fields around the crack tip under opening mode (tensile) loading can be defined as follows:

$$\begin{Bmatrix} u_x \\ u_y \end{Bmatrix} = \sum_{p=1}^{\infty} \frac{r_2^{\frac{p}{2}}}{2G} a_p \begin{Bmatrix} \left(\kappa + \frac{p}{2} + (-1)^p\right)\cos\frac{p\theta}{2} - \frac{p}{2}\cos\frac{(p-4)\theta}{2} \\ \left(\kappa - \frac{p}{2} - (-1)^p\right)\sin\frac{p\theta}{2} + \frac{p}{2}\sin\frac{(p-4)\theta}{2} \end{Bmatrix} \tag{1}$$

where u_x and u_y are respectively the horizontal and vertical components of the displacement field; r and θ are polar coordinates over an xy plane centered at the crack tip; G is the shear modulus; p is a sum index; κ is a function of Poisson's coefficient, which depends on the stress state (2D or 3D); and a_p is the half crack length for a through-thickness crack. The first coefficient of the sum is related to the Mode I SIF, K_I while the second coefficient is related to the non-singular stress in the x direction (the T-stress), $\sigma_{0x} = 4a_2$. Higher order terms can be neglected if only the singularity zone is being analyzed and no significant plastic deformation at the crack tip occurs. Moreover, if only the first two terms are considered, the Williams' model is equivalent to the Irwin–Westergaard model.[2,3] Under plane stress conditions, the out-of-plane displacement component normal to the crack plane is given by Equation 2.

$$u_z = -2z\frac{G(1+\nu)}{\nu}(\sigma_x + \sigma_y) \tag{2}$$

where z is the out-of-plane coordinate and σ_x and σ_y are the normal stresses in the horizontal and vertical directions. Conventionally, the x-axis is the crack growth direction, and the y-axis is the crack opening direction under tensile loading.

2.2 | Tangential directions and Frenet trihedral

When a non-planar curved surface is under consideration, it can be parametrized as a function of two parameters ξ and η which represent two orthogonal directions. Each point at the surface can be defined by a position vector $\vec{\rho}$ referred to a general Cartesian reference system (x, y, z) as shown in Figure 1. For a particular surface point, Q, three tangent directions can be defined by three orthogonal unity vectors (tangential, $\vec{T}$, binormal, $\vec{B}$, and normal, $\vec{N}$) according to the Frenet–Serret formulation, which gives an innate geometric description of a curve.[24] These three vectors are calculated from the position vector and the parameters ξ and η as shown in Equations 3, 4, and 5.

$$\vec{T} = \frac{\frac{\partial\vec{\rho}}{\partial\xi}}{\left\|\frac{\partial\vec{\rho}}{\partial\xi}\right\|} = \frac{\frac{\partial x}{\partial\xi}\vec{e_x} + \frac{\partial y}{\partial\xi}\vec{e_y} + \frac{\partial z}{\partial\xi}\vec{e_z}}{\sqrt{\left(\frac{\partial x}{\partial\xi}\right)^2 + \left(\frac{\partial y}{\partial\xi}\right)^2 + \left(\frac{\partial z}{\partial\xi}\right)^2}} \tag{3}$$

$$\vec{B} = \frac{\frac{\partial\vec{\rho}}{\partial\eta}}{\left\|\frac{\partial\vec{\rho}}{\partial\eta}\right\|} = \frac{\frac{\partial x}{\partial\eta}\vec{e_x} + \frac{\partial y}{\partial\eta}\vec{e_y} + \frac{\partial z}{\partial\eta}\vec{e_z}}{\sqrt{\left(\frac{\partial x}{\partial\eta}\right)^2 + \left(\frac{\partial y}{\partial\eta}\right)^2 + \left(\frac{\partial z}{\partial\eta}\right)^2}} \tag{4}$$

$$\vec{N} = \frac{\frac{\partial\vec{\rho}}{\partial\xi}}{\left\|\frac{\partial\vec{\rho}}{\partial\xi}\right\|} \times \frac{\frac{\partial\vec{\rho}}{\partial\eta}}{\left\|\frac{\partial\vec{\rho}}{\partial\eta}\right\|} \tag{5}$$

where $\vec{T}$, $\vec{B}$, and $\vec{N}$ are the tangential, binormal, and normal unitary vectors, respectively. Double vertical bars denote the two-norm of the vector (which calculates the distance of the vector coordinate from the origin of the vector space), the operator $\times$ denotes the vector cross-product, and e_x, e_y, and e_z are the components of unit vectors in the Cartesian directions.

The lengths x' and y' over the surface along the parametrization directions, ξ and η, are obtained by integration according to Equations 6 and 7.

$$x' = \int_{\xi_0}^{\xi} \sqrt{\left(\frac{\partial x}{\partial\xi}\right)^2 + \left(\frac{\partial y}{\partial\xi}\right)^2 + \left(\frac{\partial z}{\partial\xi}\right)^2}\, d\xi \tag{6}$$

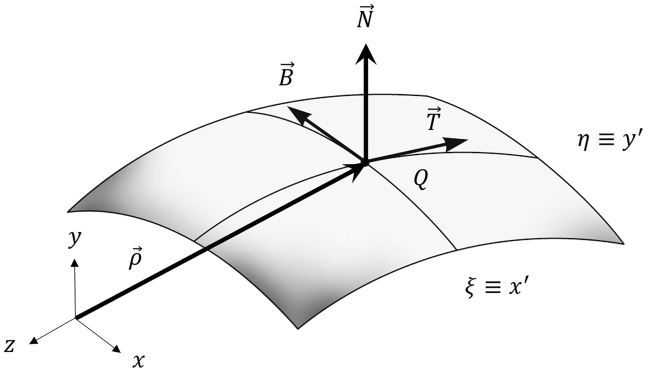

FIGURE 1 Schematic illustration showing the components of the Frenet trihedral for an arbitrary point over a generic non-flat surface[24]

$$y' = \int_{\eta_0}^{\eta} \sqrt{\left(\frac{\partial x}{\partial \eta}\right)^2 + \left(\frac{\partial y}{\partial \eta}\right)^2 + \left(\frac{\partial z}{\partial \eta}\right)^2}\, d\eta \tag{7}$$

where ξ_0 and η_0 are the integration lower limits, respectively.

2.3 | Extended crack tip model for the analysis of curved surfaces

The proposed formulation for the analysis of the crack tip field on curved surfaces assumes plane stress conditions. The objective is to combine the description provided by the curved surface crack tip field model with experimental stress and strain measurements obtained from any suitable optical technique. Thus, considering a developable surface, that is, one that can be flattened onto a plane without distortion, the normal direction given by $\vec{N}$ is the principal direction and the stress value is zero. For simplicity in illustrating the proposed methodology, a cylindrical surface containing a central circumferential crack has been considered (Figure 2A). The parametric ξ and η directions have been chosen to be respectively coincident with the crack growth and opening directions. In addition, the surface can be geometrically unwrapped over a $\xi-\eta$ plane as schematically illustrated in Figure 2B. Hence, as for the case of a two-dimensional flat surface, the Williams model can be reformulated to account for the effect of the curvature in the unwrapped surface (Equations 5 and 6). As indicated in Figure 2, the displacement in the horizontal direction (crack growth direction) is replaced by the displacement in the tangential direction, while the displacement in the vertical direction (crack opening direction) is replaced by the displacement in the binormal direction. Similarly, the rectilinear coordinates of the surface points are replaced by the curvilinear coordinates.

$$\begin{Bmatrix} u_T \\ u_B \end{Bmatrix} = \sum_{p=1}^{\infty} \frac{r'^{\frac{p}{2}}}{2G} a_p \begin{Bmatrix} \left(\kappa + \frac{p}{2} + (-1)^p\right)\cos\frac{p\theta'}{2} - \frac{p}{2}\cos\frac{(p-4)\theta'}{2} \\ \left(\kappa - \frac{p}{2} - (-1)^p\right)\sin\frac{p\theta'}{2} + \frac{p}{2}\sin\frac{(p-4)\theta'}{2} \end{Bmatrix} \tag{8}$$

$$u_N = -2z_n \frac{G(1+\nu)}{\nu}(\sigma_T + \sigma_B) \tag{9}$$

where u_T, u_B, and u_N are the displacement components in the tangential, binormal, and normal directions, respectively. If the surface is unwrapped over a plane, r' and θ' are the polar coordinates of a point Q referred to a Cartesian reference system $x'-y'$ (Figure 2B), z_n is the normal coordinate in the unwrapped plane (out-of-plane direction), and σ_T and σ_B are the normal stresses along tangential and binormal directions, respectively. The displacement components u_T, u_B, and u_N are calculated by projecting the displacement vector $\vec{u}$ at each direction defined by the Frenet trihedral as shown in Equations 10 to 12.

$$\begin{aligned} u_T &= \vec{u}\cdot\vec{T} \\ &= \left(u_x\cdot\vec{e_x} + u_y\cdot\vec{e_y} + u_z\cdot\vec{e_z}\right)\cdot\left(T_x\cdot\vec{e_x} + T_y\cdot\vec{e_y} + T_z\cdot\vec{e_z}\right) \end{aligned} \tag{10}$$

$$\begin{aligned} u_B &= \vec{u}\cdot\vec{B} \\ &= \left(u_x\cdot\vec{e_x} + u_y\cdot\vec{e_y} + u_z\cdot\vec{e_z}\right)\cdot\left(B_x\cdot\vec{e_x} + B_y\cdot\vec{e_y} + B_z\cdot\vec{e_z}\right) \end{aligned} \tag{11}$$

$$\begin{aligned} u_N &= \vec{u}\cdot\vec{N} \\ &= \left(u_x\cdot\vec{e_x} + u_y\cdot\vec{e_y} + u_z\cdot\vec{e_z}\right)\cdot\left(N_x\cdot\vec{e_x} + N_y\cdot\vec{e_y} + N_z\cdot\vec{e_z}\right) \end{aligned} \tag{12}$$

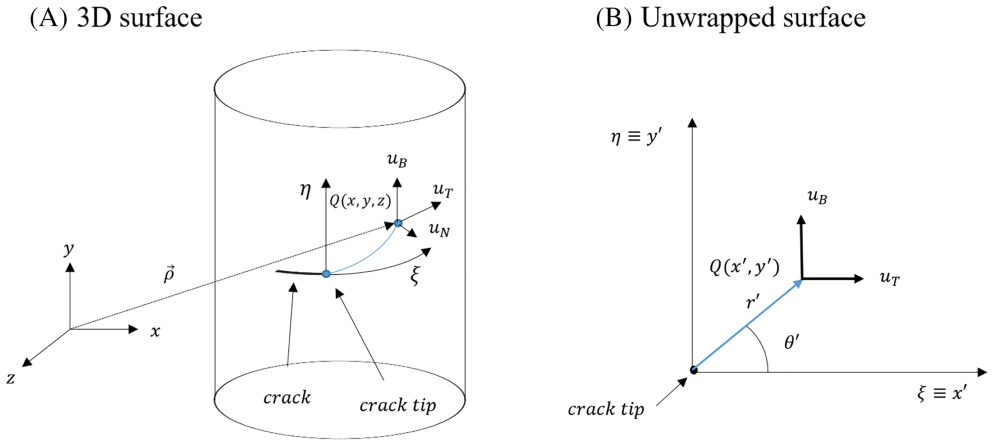

FIGURE 2 Figure to illustrate the analogy with flat models. Cracked surface (A, 3D surface) and the equivalent system on the unwrapped plane (B, unwrapped surface) [Colour figure can be viewed at wileyonlinelibrary.com]

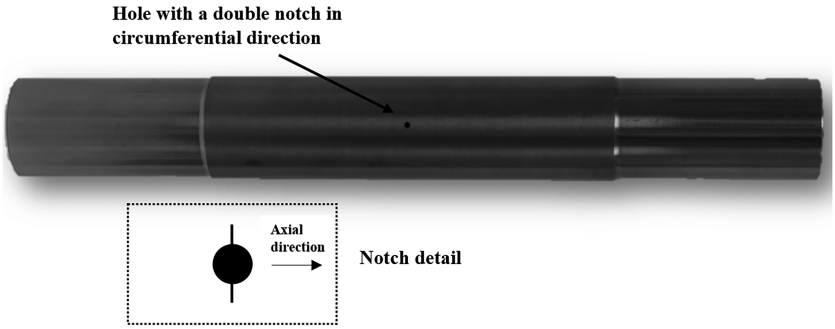

FIGURE 3 304L-SS specimen used during fatigue experiments

TABLE 1 Chemical composition of both alloys (wt %)

304L	0.02 C	0.39 Si	1.37 Mn	0.001 S	0.029 P	8.01 Ni	18.15 Cr	
2024-T3	3.8 Cu	0.1 Cr	0.3 Mn	0.5 Fe	1.2 Mg	0.5 Si	0.15 Ti	0.25 Zn

TABLE 2 Mechanical properties of the alloys

Mechanical property	Units	304L	2024-T3
Young modulus	MPa	197,000	73,100
Poisson ratio	Dimensionless	0.33	0.33
Yield stress	MPa	312	355
Ultimate tensile stress	MPa	646	483
Elongation at failure	%	53	18

3 | EXPERIMENTAL DETAILS

The proposed approach was validated by fatigue crack growth rate testing using cylindrical seamless tubes with centrally introduced notches as shown in Figure 3. Specimens were machined from either 304L austenitic stainless steel or 2024-T3 aluminum alloy. The chemical composition and mechanical properties of the two alloys are given in Tables 1 and 2. The specimens were designed and manufactured according to ASTM standard E-606-92,[25] with a length of 203.2 mm and a thickness of 2.11 mm. To suit the available material, the external diameter of the 304L specimens was 26.8 mm and that of the 2024-T3 specimens was 25.4 mm. The central notch (Figure 3) was machined from an initial drilled through-thickness hole extended with a 0.1-mm sawn slot in the circumferential direction. Crack length was calculated in radians, as the ratio between the circumferential angle subtended by the crack divided by the complete circumference (2π radians). The normalized initial notch length was 0.02 (equivalent to a crack length along the outer circumference of 1.7 mm, or 1.5° expressed in terms of the crack angle) and was chosen to provide a good resolution of the crack tip field even for very short cracks. However, the notch manufacturing process left residual stresses that affected the crack tip field at short crack lengths (in the range of normalized crack lengths from approximately 0.02 to 0.15). A 100-kN servohydraulic testing machine (MTS Landmark 370.10) was used in the fatigue tests with constant amplitude tensile loading at 10 Hz. The stress ratio was 0.525, in order to avoid any influences of crack wake closure in the measured crack tip field.[10,26] The maximum applied load was selected to ensure that SIF values were significantly higher than the threshold range[16,26] for fatigue crack growth. Hence, the maximum applied load was 30% of the yield stress for stainless steel and 20% for the aluminum specimens.

The specimen surface was prepared for the DIC work by spraying it with a stochastic black speckle pattern on a white background. Crack tip displacement fields were recorded using a 3D-DIC technique.[12] 3D-DIC can record the three-dimensional surface displacement field on the specimen, allowing calculation of the experimental SIF at maximum load for a given crack length. Experimental data were acquired with a stereoscopic vision system comprising three 5-megapixel monochrome CCD cameras each fitted with a zoom lens (MLH-10X EO) to increase the spatial resolution around the crack tip. The required depth of field to avoid blurring in the image was set via the lens aperture, with smaller apertures giving greater depth of field. A dual point fiber optic light guide was used to achieve a uniform illumination pattern around the initial notch on both sides of the specimen. The experimental set-up is shown in Figure 4.

A calibration grid (a rectangle comprising 9 × 6 dots with a 2-mm spacing between dots)[27] was used to calibrate the stereoscopic system and calculate the relative position and distance between the cameras and the specimen surface.[12] This calibration process was particularly important when measuring the very small displacements

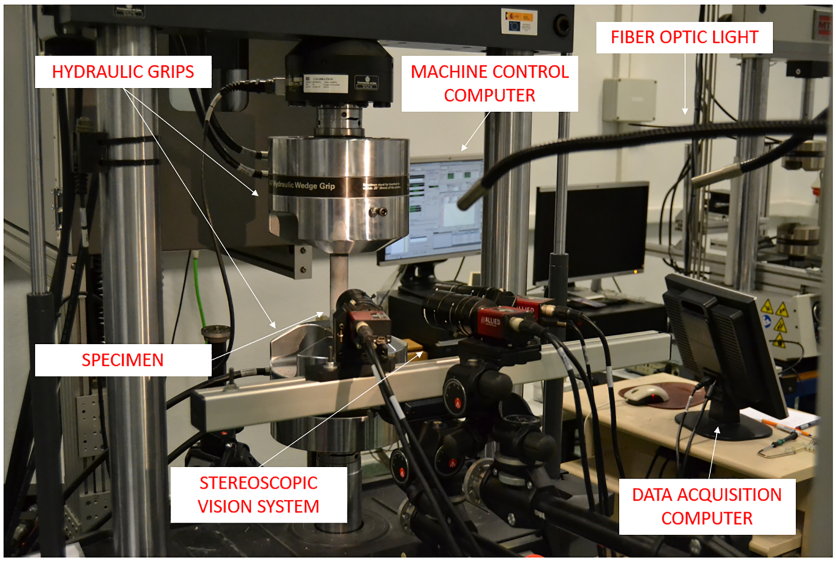

FIGURE 4 Experimental set-up [Colour figure can be viewed at wileyonlinelibrary.com]

associated with small crack lengths, and an average spatial resolution of 0.02 mm/pixel was achieved. That average spatial resolution was computed as the mean value of the distance between the adjacent points in a domain. In order to capture all possible movements of the non-planar specimen surface during a test, it was important to account for any motion of the calibration plate (either rotation or displacements) that might occur during the calibration process. DIC processing used a square subset facet size of 29 pixels with an overlap of one pixel, as this was found to reliably provide the required displacement field information.

4 | DISPLACEMENT FIELD MEASUREMENT

The crack tip displacement field under maximum load at various crack lengths was measured using the previously described 3D-DIC set-up and the commercial software VIC-3D from Correlated Solutions Inc. The measured surface displacement field together with the spatial coordinates of the central point of the facets allowed calculation of the directions of the Frenet trihedral. Figure 5 gives the measured displacement values in the Frenet binormal and tangential directions. Note that normalized crack length in radians has been used in this figure, defined as the ratio of the half angle subtended by the crack γ/π. For the chosen geometry, the crack growth direction corresponded with the circumferential direction while the crack opening direction corresponded with the axial direction since the applied load was perpendicular to the crack plane. Using Equations 3 to 7, the unitary transformation vectors and the coordinates of the unwrapped surface relative to the crack tip were calculated. Note that for the particular case considered, the transformation performed is equivalent to the use of a cylindrical (polar) coordinate system. Circumferential and axial directions were calculated from the relative position between the surface points and the directional derivatives were calculated using a finite difference approach. To reduce the error arising from the discretization process, the first derivative was calculated using a second-order finite difference approach (central derivative). Computation of the distance between points at the specimen surface used a numerical integration approach based on the compound trapezium rule. Hence, the transformation parameters were calculated corresponding to the unwrapped surface of the displacement field. Figure 5 shows tangential and binormal displacement components over the unwrapped plane for a particular crack length of 19.71 mm. Figure 5A.1,B.1 shows both displacement components in a three-dimensional plot while Figure 5A.2,B.2 shows both displacements on a map plot.

In order to extract singularity characterizing parameters from the displacement field, the Multi-Point Over-Deterministic Method (MPODM) developed by Sanford and Dally[28] was used. Mathematical fitting was performed using a mesh of points in an annular region around the crack tip (see Figure 6). This annulus avoided the plastic enclave surrounding the crack tip so that LEFM parameters could be determined. Previous work[10] has shown that the choice of mask shape, that is, rectangular or circular, does not significantly affect the results and a circular mask is easier to implement and define in data collection terms. The inner mesh radius was computed using the Dugdale[29] plastic zone radius approximation. The outer radius value was chosen in order to capture the singularity zone. Thus, according to some

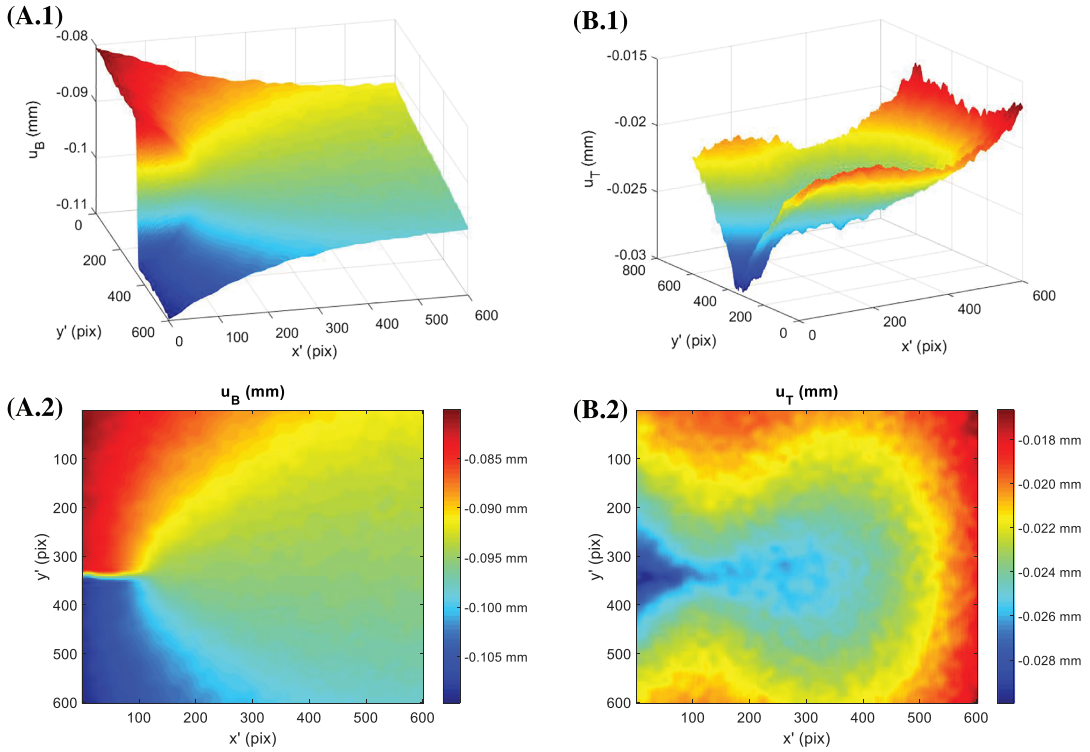

FIGURE 5 Displacement field around the crack tip in terms of binormal and tangential directions at maximum load for a crack length of 19.7 mm (normalized crack length $\gamma/\pi = 0.2377$). (A) Binormal and (B) tangential components. 304L-SS [Colour figure can be viewed at wileyonlinelibrary.com]

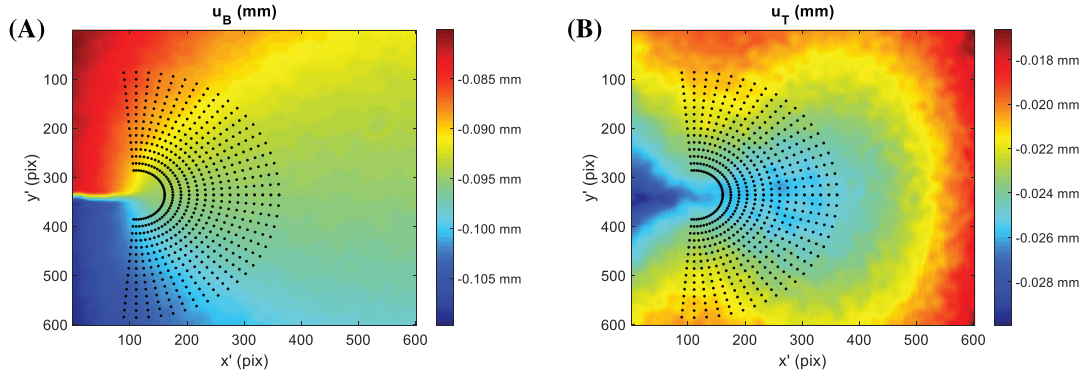

FIGURE 6 Annular mesh for data collection. (A) binormal displacement map and (B) tangential displacement map [Colour figure can be viewed at wileyonlinelibrary.com]

previous works,[6,16] a value around 40% of the crack length was chosen. Mesh points were defined linearly and therefore were equally spaced. Crack tip singularity parameters were then computed by solving a linear system of equations (with a suitable matrix factorization) using the measured surface displacements (u_T and u_B) at selected locations around the crack tip and their relative position in the unwrapped plane (x' and y'). The influence of the number of terms in the crack tip stress equations on the quality of the mathematical fitting and its effect on the calculated SIF was also evaluated. As discussed in Section 2, most crack tip stress/displacement models are formulated assuming that the crack tip is at the origin of the reference coordinate system. In the current analysis, the center of the annular mesh was placed at an initial location estimated from the observation of the measured displacement field. That initial point can be located easily and precisely since the crack path can be recognized in both maps. To locate the precise crack tip position on the unwrapped plane, a search grid was

defined over the plane as shown in Figure 7. For each point of the grid, which are defined by their coordinates x_i' and y_i', an error function F_i was formulated (Equation 13). The model was then fitted to the experimental data at each point of the grid and the minimum value of the error function was used to determine the crack tip location.[30,31] These positions were then used to calculate SIFs. Hence, from the mathematical fitting, coefficients that describe the crack tip fields could be obtained and the opening mode SIF K_I calculated.

$$F = \sqrt{\left\| \frac{u_T^{th} - u_T^e}{u_T^{th}} \right\|^2 + \left\| \frac{u_B^{th} - u_B^e}{u_B^{th}} \right\|^2} \tag{13}$$

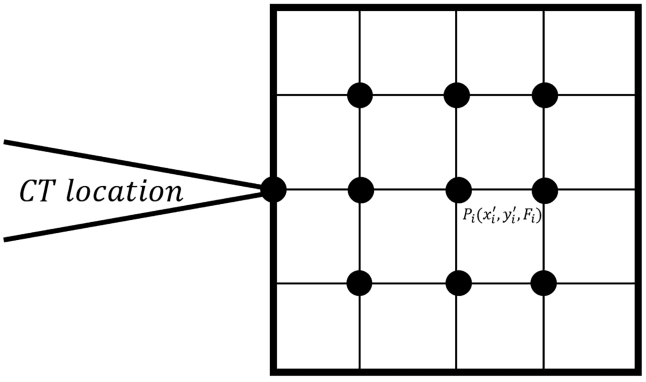

FIGURE 7 Search grid for crack tip localization

where double vertical bars indicate the operator norm and superscripts *e* and *th* refer to experimental and theoretical displacement data, respectively.

To validate the accuracy of the plane stress assumption at the specimen surface, displacement fields in the normal direction were obtained experimentally and theoretically (the latter via mathematical fitting) and compared. Once crack tip parameters were calculated, the displacement field in the normal direction could be calculated (Equation 6) and compared with that measured using 3D-DIC. This comparison was also made for SIFs, where calculated experimental values were compared with values calculated from empirical correlations reported by Tada et al[23] based on Sanders' results.[21,22]

It should be noted that for the stainless steel, the crack grew from the notch on a single side of the specimen, while in the case of the aluminum alloy cracks grew from both notches, as indicated in Figure 8. The crack topology in the two different materials therefore corresponds to different empirical correlations. Tada's correlation[21–23] for a single crack (304L-SS) is given by Equation 14, and for the case of a double crack (2024-T3-Al), Equation 15 is applicable.

$$K_I = \frac{P}{2\pi R t}\sqrt{R}\left(\frac{\sqrt{2}}{\left(\frac{t}{R\sqrt{12(1-\nu^2)}}\right)^{\frac{1}{2}}}\right)^{\frac{1}{2}}\left(\gamma + \frac{1-\gamma\cdot\cos\gamma}{2\cot\gamma + \sqrt{2}\cot\left(\frac{\pi-\gamma}{\sqrt{2}}\right)}\right) \tag{14}$$

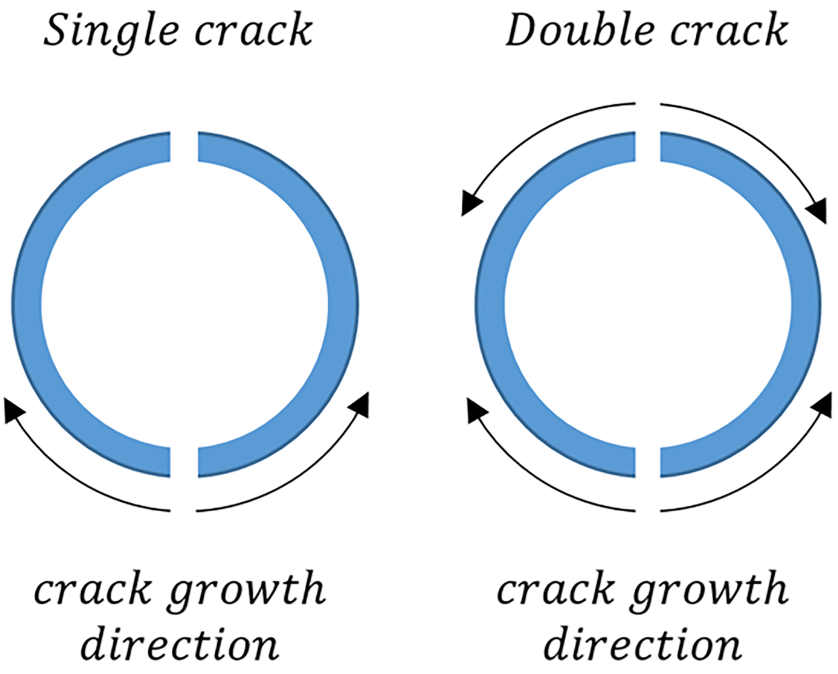

FIGURE 8 Schematic illustration showing how the crack was growing during fatigue test for the two materials tested during fatigue experiments, left) single crack corresponding to 304L-SS and (right) double crack corresponding to 2024-T3-Al [Colour figure can be viewed at wileyonlinelibrary.com]

$$K_I = \sqrt{\frac{\tan\gamma}{\gamma}}\frac{P}{2\pi Rt}\sqrt{\pi R\gamma} \tag{15}$$

In these expressions, P is the axial load, R is the mean radius of the cylindrical specimen, t is the wall thickness, ν is Poisson's ratio, and γ is the subtended half angle of the crack. The crack length was measured as the distance over the specimen surface between the crack tip location and the center of the original starter hole. In addition, the crack angle was calculated as the ratio between the curved surface crack length and the outer radius of the cylinder. To assess the quality of the proposed methodology in describing the crack tip field, a comparison was made between the experimental and theoretically fitted displacement field in terms of the SIF confidence intervals and their relative fitting error.

5 | RESULTS AND DISCUSSION

Experimental data were fitted to the Williams model using the methodology described above while also sequentially increasing the number of terms used in the expansion series. In the present work, beyond four terms, the model output became stable, and the magnitude of higher order terms was negligible (less than 10^{-16}). This is indicative of a high quality correlation between the experimental and the mathematically fitted data. Furthermore, the SIF values obtained using a reduced number of terms did not change significantly as the number of terms was increased. The resultant Mode I SIF values calculated using 2, 3, and 4 terms in the Williams' expansion series as a function of the normalized crack length are shown in Figure 9 for 304L-SS and in Figure 10 for 2024-T3-Al. The reliability of the results was also illustrated via a comparison with the nominal values of K_I calculated according to Equations 14 and 15 (Figures 9 and 10) and showed a high level of agreement, with average errors for the 304L alloy of only 6.36%, 5.38%, and 4.13% using 2, 3, and 4 terms, respectively, and 3.18%, 3.74%, and 3.18% for 2, 3, and 4 terms in the case of the 2024-T3 alloy.

These small differences can be explained by the presence of noise inherent to the DIC stereoscopic calibration residuals and the differentiation process that occurs when implementing the proposed approach. Moreover, the use of average values in the elastic constants could also modify the results by around 1% (the range of Young's modulus provided by the alloy manufacturer).

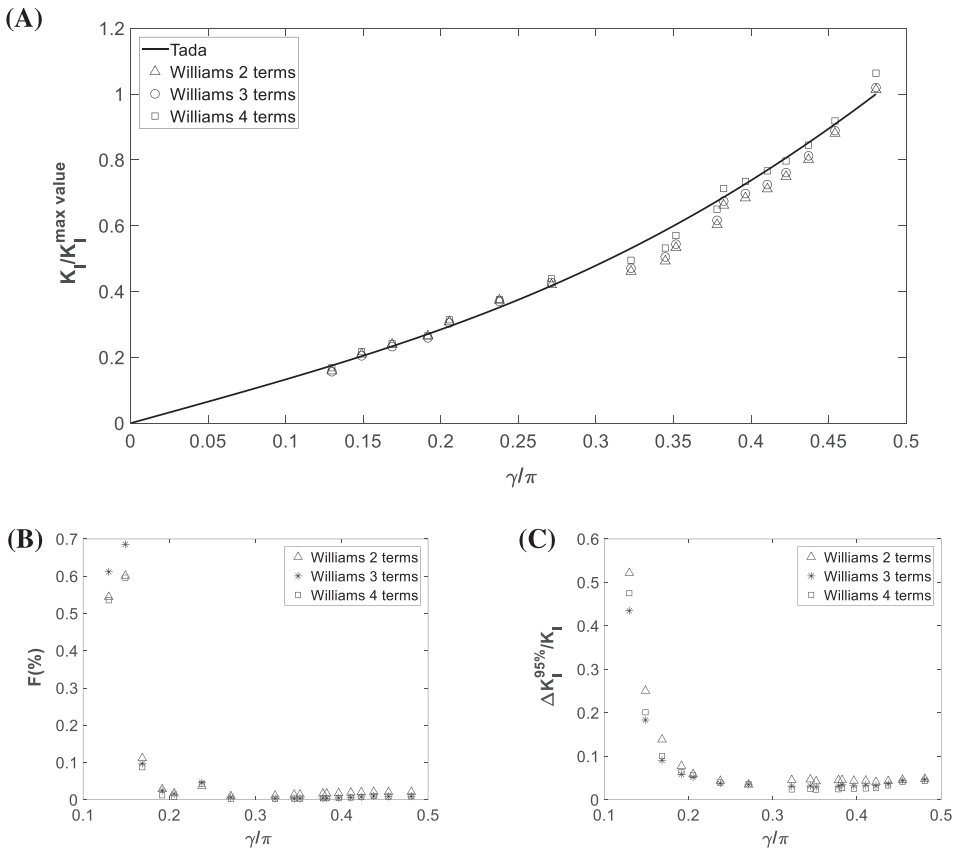

FIGURE 9 Variation with the normalized crack length and the number of terms in the Williams stress series expansion used in the calculations, as a function of (A) the ratio between the calculated and the standard expression stress intensity factors; (B) relative fitting error between the calculated and standard SIF values; and (C) the ratio between the stress intensity factor range within a 95% confidence interval and the standard stress intensity factor values for 304L-SS

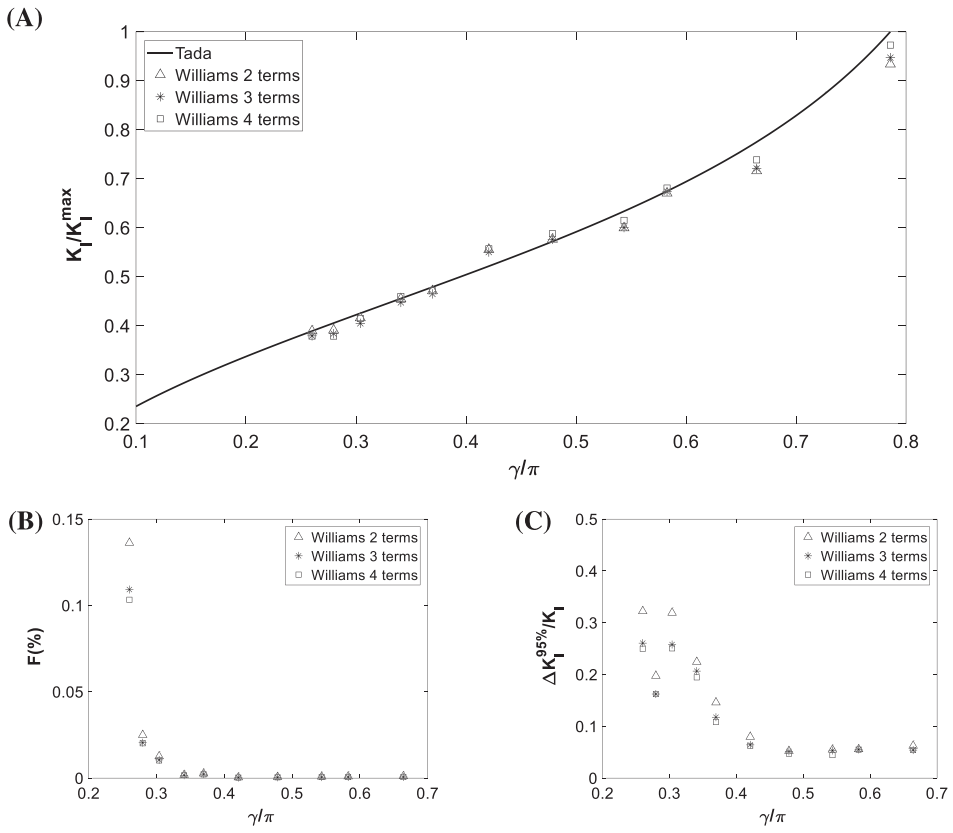

FIGURE 10 Variation with the normalized crack length and the number of terms in the Williams stress series expansion used in the calculations, as a function of (A) the ratio between the calculated and the standard expression stress intensity factors; (B) relative fitting error between the calculated and standard SIF values; and (C) the ratio between the stress intensity factor range within a 95% confidence interval and the standard stress intensity factor values for 2024-T3-Al

Equally, however, standard SIF correlations do not consider any effect of crack tip plasticity during fatigue crack growth and, consequently, their values may differ slightly from the experimental values calculated using the present hypothesis. Nonetheless, the mathematical model developed to perform the stress field fitting is also based on linear elastic fracture mechanics, thus any shielding effect due to crack tip plasticity is not explicitly considered.

The accuracy of the mathematical fitting together with the relative error in the fitting process (given by the error function defined in Equation 13) and the dimensionless range of the 95% confidence intervals around the results are illustrated in Figure 9 and 9C for the 304L alloy and in Figure 10B,C for the 2024-T3 alloy. These parameters in both materials show similar trends with a higher fitting error of between 0.4% and 0.7% at shorter crack lengths, followed by an exponential decrease to a stable lower value of ≈0.005%. It is believed that these initial higher values seen with short cracks (normalized crack lengths between 0.1 and 0.15) reflect the influence on the initial crack tip field of residual stresses generated during notch machining. In all cases, the maximum error was <1%. The upper limit of the model in terms of normalized crack length, as indicated in Figures 9 and 10, is around 0.5 for 304L alloy and 0.7 for the 2024-T3 alloy. This upper limit occurs because the displacement fields at longer crack lengths are not adequately described by the Williams crack field equations, since the specimen ligament was fully plastic. Thus, a limitation on applicability of the proposed model arises from excessive plasticity (large-scale yielding conditions) in the remaining uncracked ligament in the specimen.

However, the results obtained clearly illustrate the ability of the proposed differential geometry method to characterize crack tip fields on non-planar elements through a two-dimensional planar model.

In addition to a quantitative evaluation of the proposed method in terms of the calculation of SIFs, it is useful to show a direct comparison between the displacement values measured at the fitting locations superimposed on the reconstructed 3D surface displacement field obtained using Williams' analytical model with the fitting coefficients obtained at various normalized crack lengths (as shown in Figures 11 and 12). These figures clearly illustrate three aspects of the proposed model (the binormal displacement in the figures A.1 to A.3 and the tangential displacement in figures B.1 to B.3). Firstly, the number of terms used in the Williams stress expansion does not have any significant effect on the observed agreement between the experimental data and the reconstructed displacement field. Secondly, at short crack lengths, data dispersion is higher than seen for longer cracks and, as previously discussed, this is attributed to

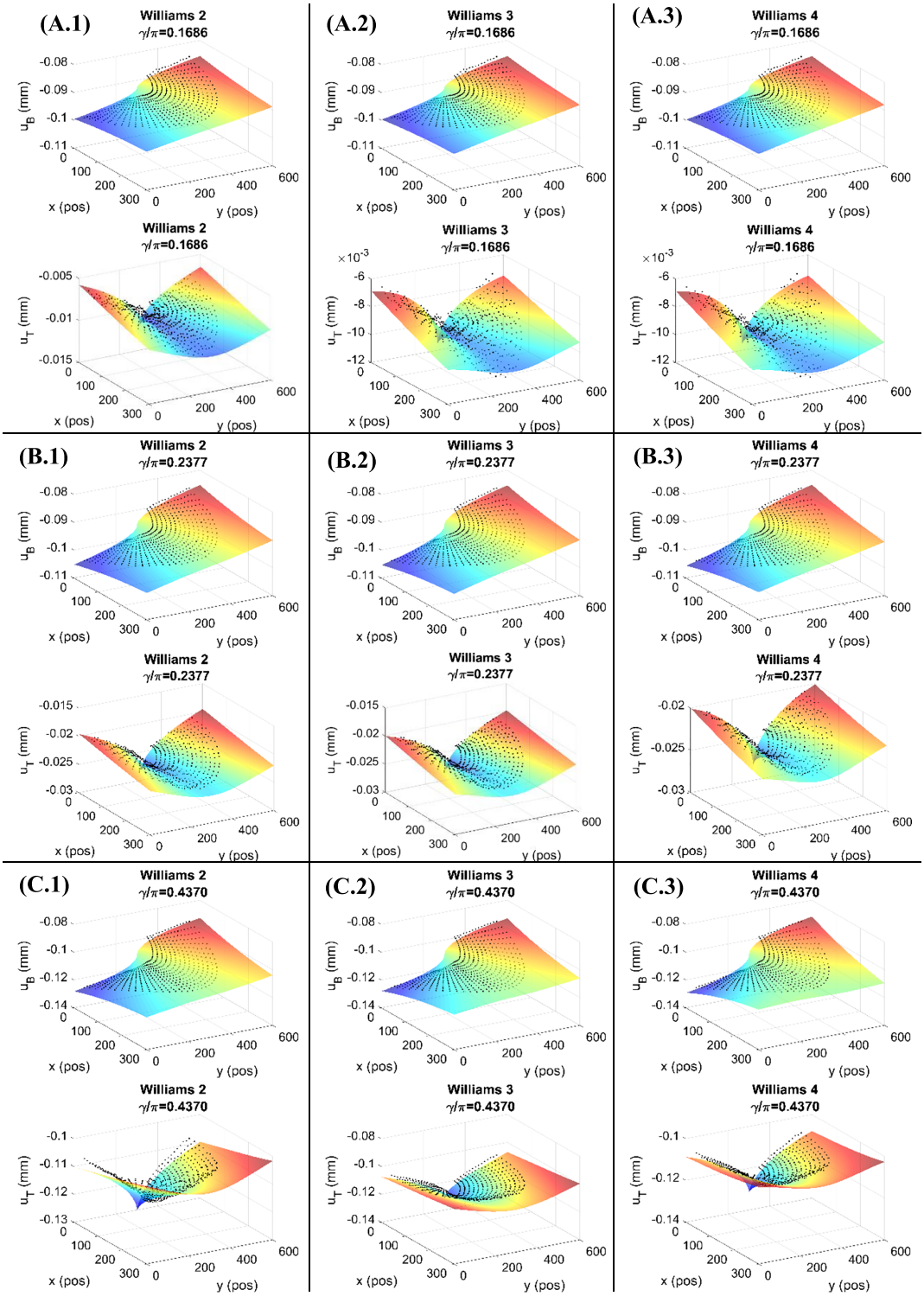

FIGURE 11 304L alloy: Comparison between the experimentally measured and the fitted crack tip displacement fields (tangential and binormal) as a function of normalized crack length and the number of terms used in the mathematical fitting; (A), (B), and (C) refer to normalized crack lengths γ/π, of 0.1686, 0.2377, and 0.4370, while 1, 2, and 3 identify the number of stress expansion terms used, that is, 2, 3, and 4 [Colour figure can be viewed at wileyonlinelibrary.com]

notch-induced residual stresses. Finally, as crack length increases, the tangential component changes more significantly than the binormal component and this is attributed to the influence of *T*-stress, whose value increases as the uncracked ligament is reduced (far-field boundary effect).[32]

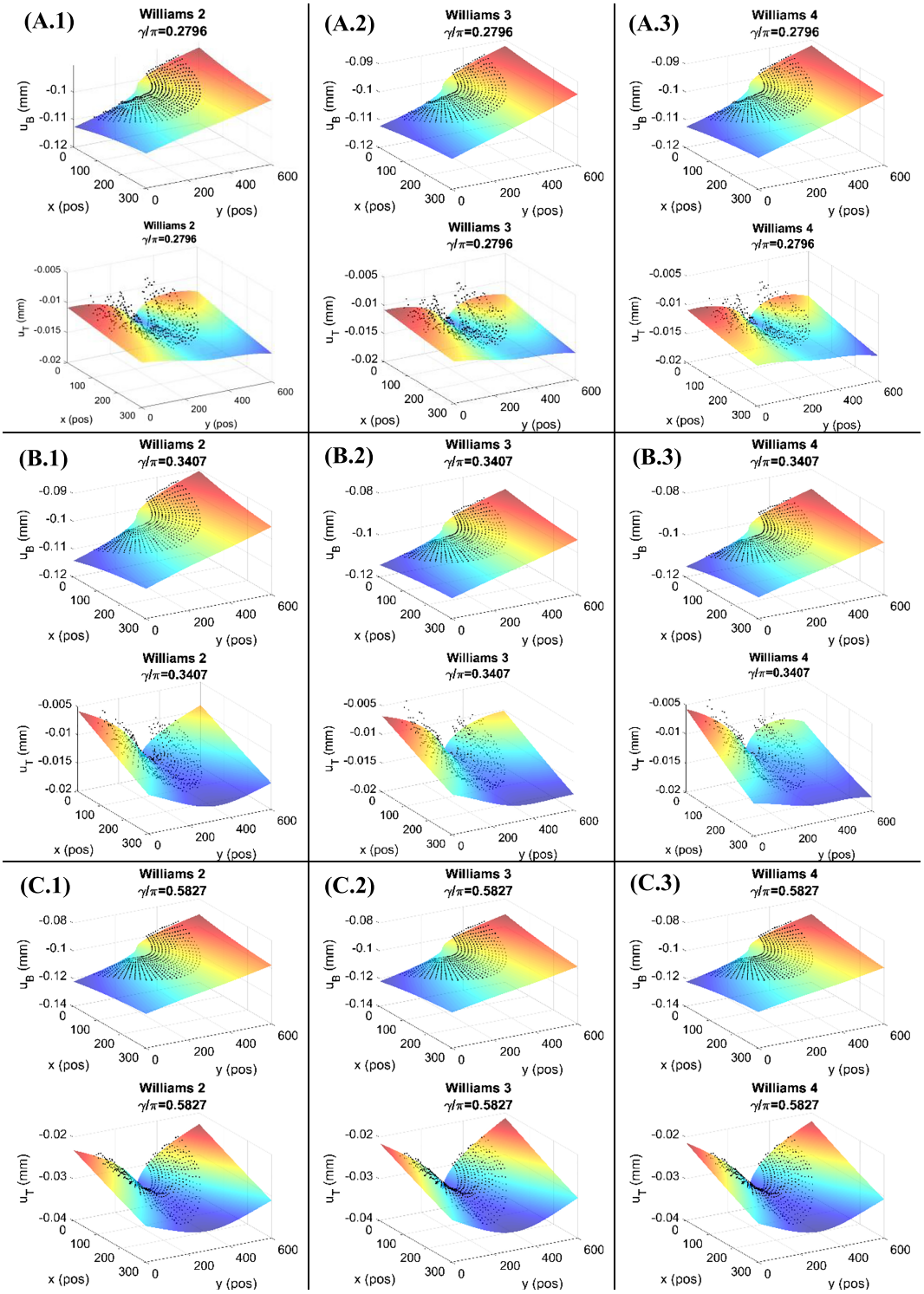

FIGURE 12 2024-T3 alloy: Comparison between the experimentally measured and the fitted crack tip displacement fields (tangential and binormal) as a function of normalized crack length and the number of terms used in the mathematical fitting; (A), (B), and (C) refer to normalized crack lengths γ/π, 0.2796, 0.3407, and 0.5827, while 1, 2, and 3 identify the number of stress expansion terms used, that is, 2, 3, and 4 [Colour figure can be viewed at wileyonlinelibrary.com]

To summarize this work, experimentally measured 3D displacement fields have been compared using a mathematically fitted 2D model, in order to demonstrate that the specimen surface experiences plane stress conditions. Using the fitting coefficients obtained in the process, the tangential and binormal stresses were

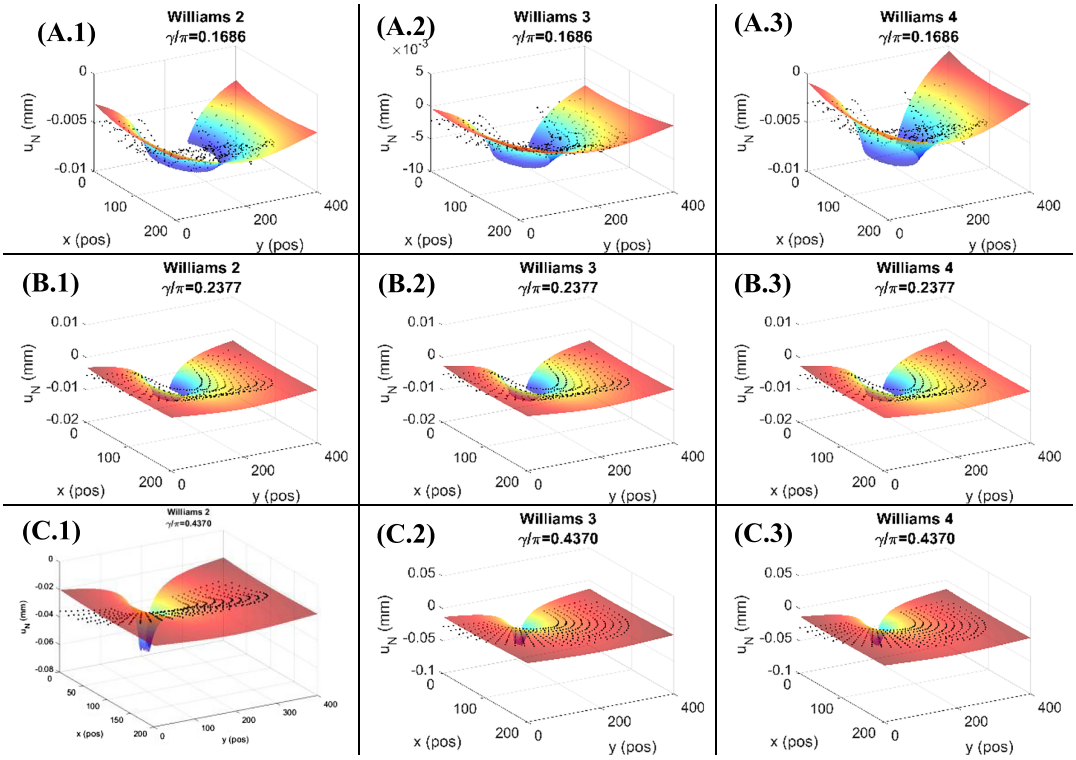

FIGURE 13 304L alloy: Comparison between measured and fitted normal displacements as a function of the normalized crack length and the number of terms used in the mathematical fitting; (A), (B), and (C) refer to normalized crack lengths of 0.1686, 0.2377, and 0.4370, while 1, 2, and 3 identify the number of stress expansion terms used, that is, 2, 3, and 4 [Colour figure can be viewed at wileyonlinelibrary.com]

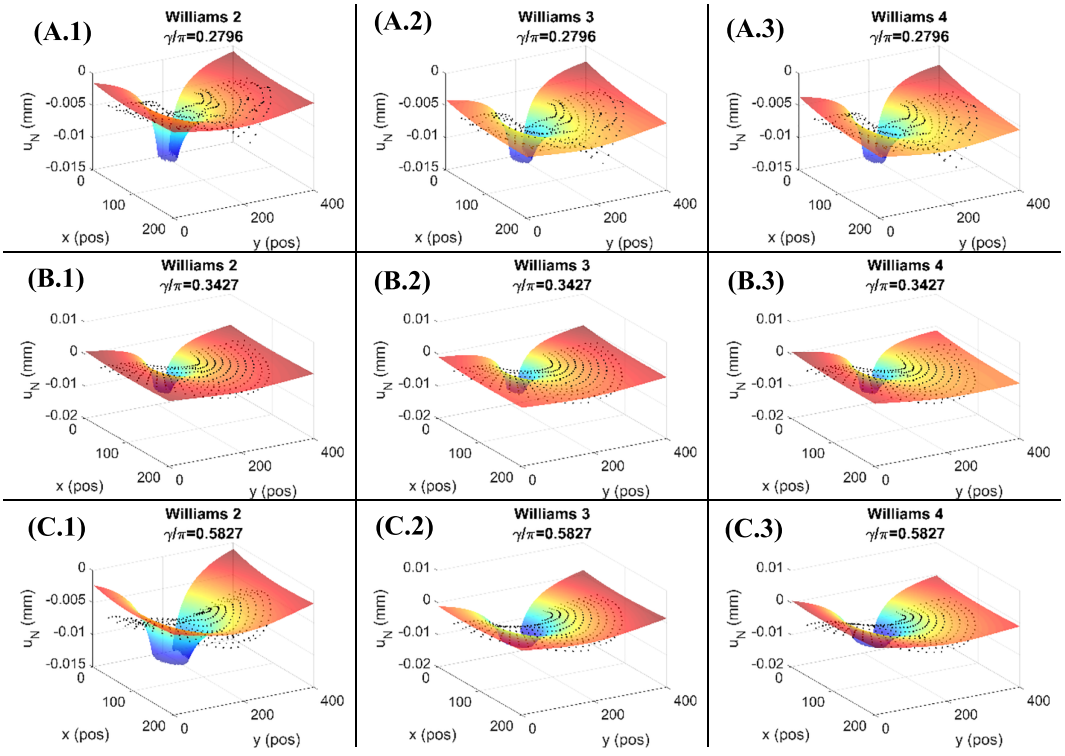

FIGURE 14 Comparison between measured and fitted normal displacements as a function of the normalized crack length and the number of terms used in the mathematical fitting; (A), (B), and (C) refer to normalized crack lengths of 0.2796, 0.3427, and 0.5827, while 1, 2, and 3 identify the number of stress expansion terms used, that is, 2, 3, and 4 [Colour figure can be viewed at wileyonlinelibrary.com]

calculated, and hence, the normal component of the stress could be found (Equation 9). In this case, the variable z_n represents the radial direction (for the particular geometry evaluated, this is the radius of the sample, 13.4 and 12.7 mm for the 304L alloy and the 2024-T3 alloy, respectively). Figures 13 and 14 show a comparison between the measured and calculated displacement field in the radial direction, and similar trends are observed in both materials. The scatter in the experimental data at shorter crack lengths reflects the influence of the residual notch manufacturing stresses, as the magnitude of the measured normal displacements was particularly small for the case of short cracks (values close to 1 μm) which emphasizes the effect of any noise arising during differentiation of the data. For longer cracks, the noise is very significantly reduced as the magnitude of the measured displacements increases. The mean relative fitting error was calculated as 7.45% and 11.25% for the stainless steel and the aluminum alloy, respectively. While these values are significantly higher than the equivalent error found in the binormal and tangential components, they seem reasonable in view of the fact that the order of magnitude of this displacement component is much lower than for the binormal or tangential, and hence, the presence of noise is more significant. Regarding the higher error in the aluminum alloy, scatter was higher due to the lower applied load levels, and in consequence, the lower displacement values.

6 | CONCLUSIONS

A novel technique has been presented in this paper for the characterization of crack tip fields on non-flat and developable surfaces. It combines a two-dimensional crack tip field model with differential geometry, and the results obtained demonstrate that crack tip fields at the surface on non-planar geometries can be accurately characterized via a modified two-dimensional planar model. In terms of SIF, the field shape and relative fitting error results demonstrate a high level of agreement between the measured and fitted displacement fields. The present paper has presented an analysis of the proposed technique under pure Mode I loading. Extending the analysis to mixed mode cracking is an obvious next step but has increased complexity due to such mixed mode phenomena such as load-path dependence, arising from crack tip plasticity. The order in which the loads are applied, as well as whether they are applied in-phase or out-of-phase, therefore influence the crack path. However, the proposed method opens up the possibility of experimentally studying fatigue and fracture problems for curved surfaces that, until now, could only be addressed analytically or numerically. This paper therefore presents a powerful tool in the analysis of cracked non-planar structural components. Although there are some limitations in the plane stress assumption, the proposed technique covers a wide range of thin-walled mechanical elements with curved geometries. One of the main advantages of this method is that the approach does not require any additional experimental validation, in contrast with numerical simulations. The ability to analyze cracked components with complex geometries using full-field optical techniques in conjunction with crack field models represents a significant advance in the subject, as there is a scarcity of experimental-analytical models suitable for addressing this kind of problem.

ACKNOWLEDGMENTS

The authors want to acknowledge the financial support from Junta de Andalucía through the research project "1380786" funded by the program "Proyectos de I + D + i en el Marco del Programa Operativo FEDER Andalucía 2014-2020. Convocatoria 2020."

CONFLICT OF INTEREST

The authors declare that they have no known competing financial interests or personal relationships that could have appeared to influence the work reported in this paper.

DATA AVAILABILITY STATEMENT

The data that support the findings of this study are available from the corresponding author upon reasonable request.

NOMENCLATURE

F	relative error fitting function
G	shear modulus
κ	function of Poisson's coefficient
K_I	Mode I stress intensity factor
p	Williams' model sum index
P	axial loading
r,θ	polar coordinates
r',θ'	polar coordinates over the unwrapped surface
Q	arbitrary 3D surface point
R	mean radius of the cylindrical pipe
t	cylindrical pipe wall thickness
T_i,B_i,N_i	component of the vector along Cartesian i direction. $i=x,y,z$
u_T,u_B,u_N	displacement field components expressed in Frenet–Serret trihedron directions
u_x,u_y,u_z	components of the displacement field
ν	Poisson's coefficient

x,y,z	Cartesian coordinates
x',y'	lengths over a 3D surface
z_n	out-of-plane direction in the unwrapped plane
a_p	coefficients of Williams' model
γ	subtended half angle of the crack
ξ,η	parametrization parameters
ξ_0,η_0	integration lower limits of the integral for computing curve lengths
σ_T,σ_B	normal stresses expressed along Frenet–Serret trihedon directions
σ_{0x}	non-singular stress in the x direction
σ_x,σ_y	normal components of the plane stress tensor
$\vec{e_x},\vec{e_y},\vec{e_z}$	unitary vectors in Cartesian axes
$\vec{\rho}$	position vector
$\vec{T},\vec{B},\vec{N}$	Frenet–Serret trihedon components

ORCID

Alonso Camacho-Reyes https://orcid.org/0000-0002-7524-0039
Jose M. Vasco-Olmo https://orcid.org/0000-0002-2250-2306
Francisco A. Diaz https://orcid.org/0000-0003-0467-542X

REFERENCES

1. Nishida SI. *Failure Analysis in Engineering Applications*. Elsevier; 1992.
2. Westergaard HM. Bearing pressures and cracks. *J Appl Mech*. 1939;61(2):49-53.
3. Irwin GR. Analysis of stresses and strains near the end of a crack traversing plate. *J Appl Mech*. 1957;24(3):361-370.
4. Williams ML. On the stress distribution at the base of a stationary crack. *J Appl Mech*. 1957;24(1):109-114.
5. Hutchinson JW. Crack tip singularity fields in non-linear fracture mechanics. *Adv Fract Res*. 1982;6:2669-2684.
6. Nurse AD, Patterson EA. Determination of predominantly mode-II stress intensity factors from isochromatic data. *Fatigue Fract Eng Mater Struct*. 1993;16(12):1339-1354.
7. Muskhelishvili NI. *Some Basic Problems of the Mathematical Theory of Elasticity*. Netherlands: Springer; 1977.
8. Pommier S, Hamam R. Incremental model for fatigue crack growth based on a displacement partitioning hypothesis of mode I elastic-plastic displacement fields. *Fatigue Fract Eng Mater Struct*. 2007;30(7):582-598.
9. Christopher CJ, James MN, Patterson EA, Tee KF. Towards a new model of crack tip stress fields. *Int J Fract*. 2007;148(4):361-371.
10. Vasco-Olmo JM, Diaz FA, Patterson EA. Experimental evaluation of shielding effect on growing fatigue cracks under overloads using ESPI. *Int J Fatigue*. 2016;83:117-126.
11. Brewster D. On the communication of the structure of doubly refracting crystals to glass, muriate of soda, flour spar and other substances by mechanical compression and dilatation. *Philos Mag*. 1816;106:156-178.
12. Schreier H, Orteu JJ, Sutton MA. *Image Correlation for Shape, Motion and Deformation Measurements: Basic Concepts, Theory and Applications*. US: Springer; 2009.
13. Thomson W. On the thermoelastic, thermomagnetic and pyroelectric properties of matters. *Philos Mag*. 1878;5(28):4-27.
14. Lopez-Crespo P, Shterenlikht A, Patterson EA, Yates JR, Withers PJ. The stress intensity of mixed mode cracks determined by digital image correlation. *J Strain Anal Eng Des*. 2008;43(8):769-780.
15. Yates JR, Zanganeh M, Tai YH. Quantifying crack tip displacement fields with DIC. *Eng Fract Mech*. 2010;77(11):2063-2076.
16. Vasco-Olmo JM, Diaz FA, Garcia-Collado A, Dorado-Vicente R. Experimental evaluation of crack shielding during fatigue crack growth using digital image correlation. *Fatigue Fract Eng Mater Struct*. 2015;38(2):223-237.
17. Vasco-Olmo JM, James MN, Christopher CJ, Patterson EA, Diaz FA. Assessment of crack tip plastic zone size and shape and its influence on crack tip shielding. *Fatigue Fract Eng Mater Struct*. 2016;39(8):969-981.
18. Diaz FA, Vasco-Olmo JM, Lopez-Alba E, Felipe-Sese L, Molina-Viedma AJ, Nowell D. Experimental evaluation of effective stress intensity factor using thermoelastic stress analysis and digital image correlation. *Int J Fatigue*. 2020;135:105567.
19. Mokhtarishirazabad M, Lopez-Crespo P, Moreno B, Lopez-Moreno A, Zanganeh M. Optical and analytical investigation of overloads in biaxial fatigue cracks. *Int J Fatigue*. 2017;100:583-590.
20. Vormwald M, Hos Y, Freire JLF, Gonzales GLG, Diaz JG. Crack tip displacement fields measured by digital image correlation for evaluating variable mode-mixity during fatigue crack growth. *Int J Fatigue*. 2018;115:53-66.
21. Sanders JL. Circumferential through-cracks in cylindrical-shells under tension. *J Appl Mech Asme*. 1982;49(1):103-107.
22. Sanders JL. Analysis of circular cylindrical-shells. *J Appl Mech Asme*. 1983;50(4b):1165-1170.
23. Tada H, Paris PC, Irwin GR. *The Stress Analysis of Cracks Handbook*. 3rded. New York: ASME Press; 2000.
24. Kobayashi S. *Differential Geometry of Curves and Surfaces*. Singapore: Springer Singapore; 2010.
25. ASTM. E 606-92: standard practice for strain-controlled fatigue testing. In: *Annual Book of ASTM Standards*. ASTM International; 1998 E-606-92.
26. Kalnaus S, Fan F, Jiang Y, Vasudevan AK. An experimental investigation of fatigue crack growth of stainless steel 304L. *Int J Fatigue*. 2009;31(5):840-849.
27. Correlates Solutions. (n.d.). Correlates solutions. Accessed January 20, 2021. https://www.correlatedsolutions.com/
28. Sanford RJ, Dally JW. A general method for determining mixed-mode stress intensity factors from isochromatic fringe patterns. *Eng Fract Mech*. 1979;621:621-633.
29. Dugdale DS. Yielding of steel sheets containing slits. *J Mech Phys Solids*. 1960;8(2):100-104.
30. Yoneyama S, Morimoto Y, Takashi M. Automatic evaluation of mixed-mode stress intensity factors utilizing digital image correlation. *Strain*. 2006;42(1):21-29.

31. Zanganeh M, Lopez-Crespo P, Tai YH, Yates JR. Locating the crack tip using displacement field data: a comparative study. *Strain*. 2013;49(2):102-115.
32. Shahani AR, Tabatabaei SA. Effect of T-stress on the fracture of a four point bend specimen. *Mater Des*. 2009;30(7):2630-2635.

How to cite this article: Camacho-Reyes A, Vasco-Olmo JM, James MN, Diaz FA. Characterization of non-planar crack tip displacement fields using a differential geometry approach in combination with 3D digital image correlation. *Fatigue Fract Eng Mater Struct*. 2022; 45(5):1521-1536. doi:10.1111/ffe.13686